

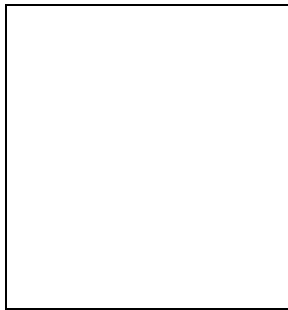
COSMIC MICROWAVE BACKGROUND ANISOTROPY IN THE *COBE* DMR 4-YR SKY MAPS

Krzysztof M. Górski^{1,2,3}

¹ *Hughes/STX, NASA/GSFC, Code 685, Greenbelt, MD 20771, USA.*

² *TAC, Juliane Maries Vej 30, 2100 Copenhagen Ø, Denmark (present address).*

³ *on leave from Warsaw University Observatory, Warsaw, Poland.*



Abstract

The *COBE* satellite has provided the only comprehensive multi-frequency full-sky observations of the microwave sky available today. Assessment of the observations requires a detailed likelihood analysis to extract the maximum amount of information present in the noisy data. I present a specific method for estimating the CMB anisotropy power spectrum independent of any assumptions about the underlying cosmology, and then use standard image processing techniques to generate the most revealing corresponding maps of the signal. The consistency of the data at the three available frequencies provides strong support to the assertion that we are being provided with our first glimpse of the last scattering surface.

1 Introduction

Operations of the Differential Microwave Radiometer instruments (DMR), the last active experiment on board NASA's COsmic Background Explorer (*COBE*) satellite, were terminated in December 1993, concluding four years of measurements of anisotropy of the cosmic microwave background (CMB) radiation. The final product of the DMR-team work — full sky maps of the microwave sky at 31.5, 53, and 90 GHz — were released to the astronomical community in January 1996. A generic description of the final DMR data set and brief summary of the results of the DMR-team analysis were given in [4]. The issues of prime concern in the DMR-team work included the following:

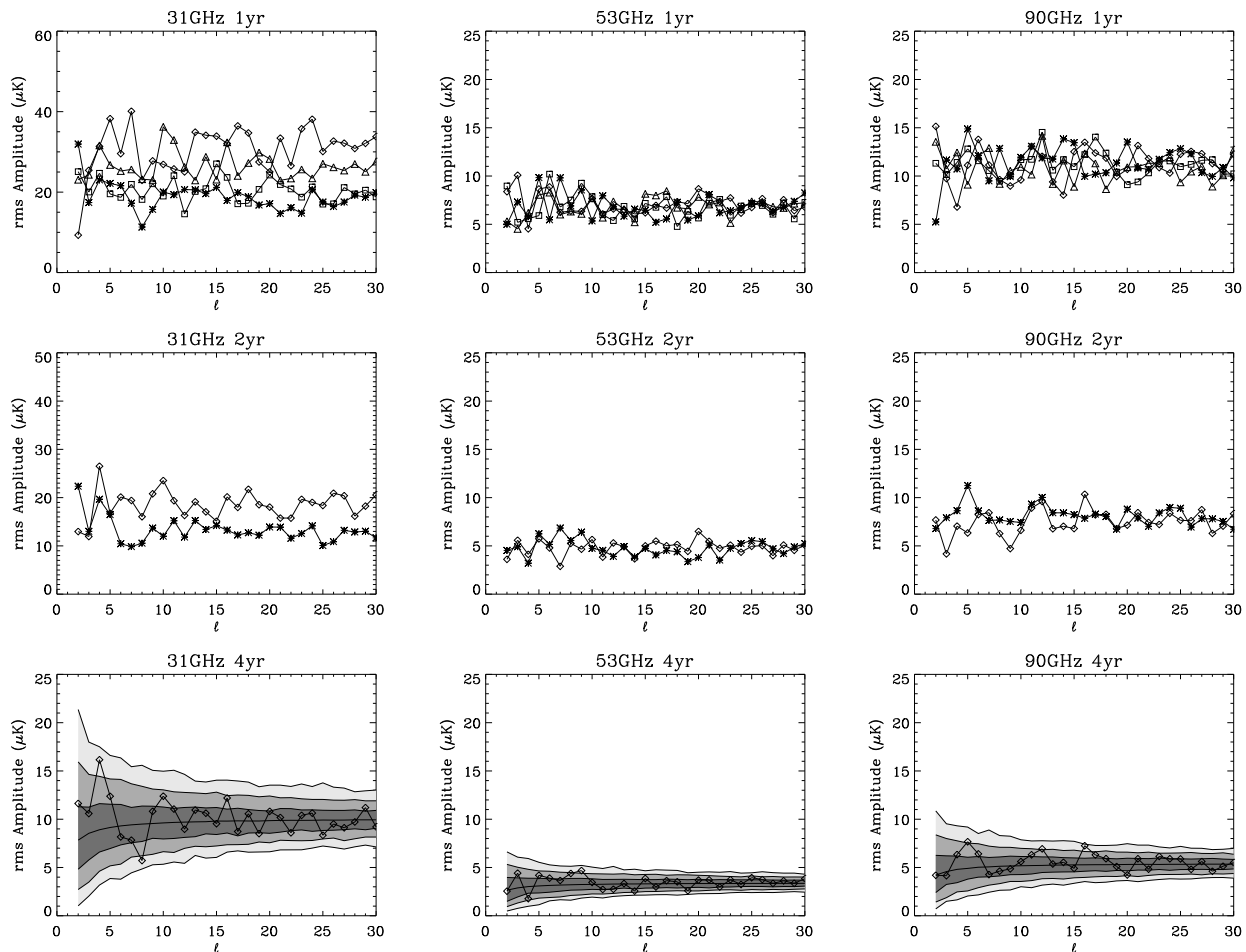


Figure 1: Power spectra of the DMR (galactic frame, extended Galaxy cut, 3881 pixels) difference maps, $(A-B)/2$, at each frequency of observations, for each yearly sky maps (top row, stars — year one, squares - year 2, triangles — year 3, diamonds — year 4), for two 2-year sky maps (middle row, stars — years 1 and 2, diamonds — years 3 and 4), and for the final four-year product (bottom row, diamonds). Bottom row plots include the 68, 95, and 99% confidence regions (heavy to light grey) from Monte Carlo simulations of instrumental noise in the sky maps.

- 1) modeling and removal of identified systematic artifacts from the data (see [13]) to produce sky maps suitable for cosmological studies,
 - 2) studies of potential signal contamination by the Galaxy [11], and/or the extragalactic sources [1],
 - 3) testing of the hypothesis of primordial origin of the measured CMB anisotropy [2] by evaluation of the frequency dependence of the $(\delta T/T)_{rms}$ in the sky maps,
 - 4) testing of the hypothesis of gaussianity of statistics of the measured anisotropies [12],
 - 5) evaluation and analysis of the auto- and cross-correlation functions of the sky maps [9],
 - 6) determination of the angular power spectrum of the CMB anisotropy [8], [10], [16].
- Other analyses of the 4 year data presented so far include [5], [15], and Bond and Jaffe in these Proceedings.

In this contribution I will focus on two aspects of the interpretation and visualisation of the COBE-DMR data: 1) derivation of the angular power spectrum of the CMB anisotropy using a data reduction method which is *independent* of the cosmological model, and 2) linear filtering

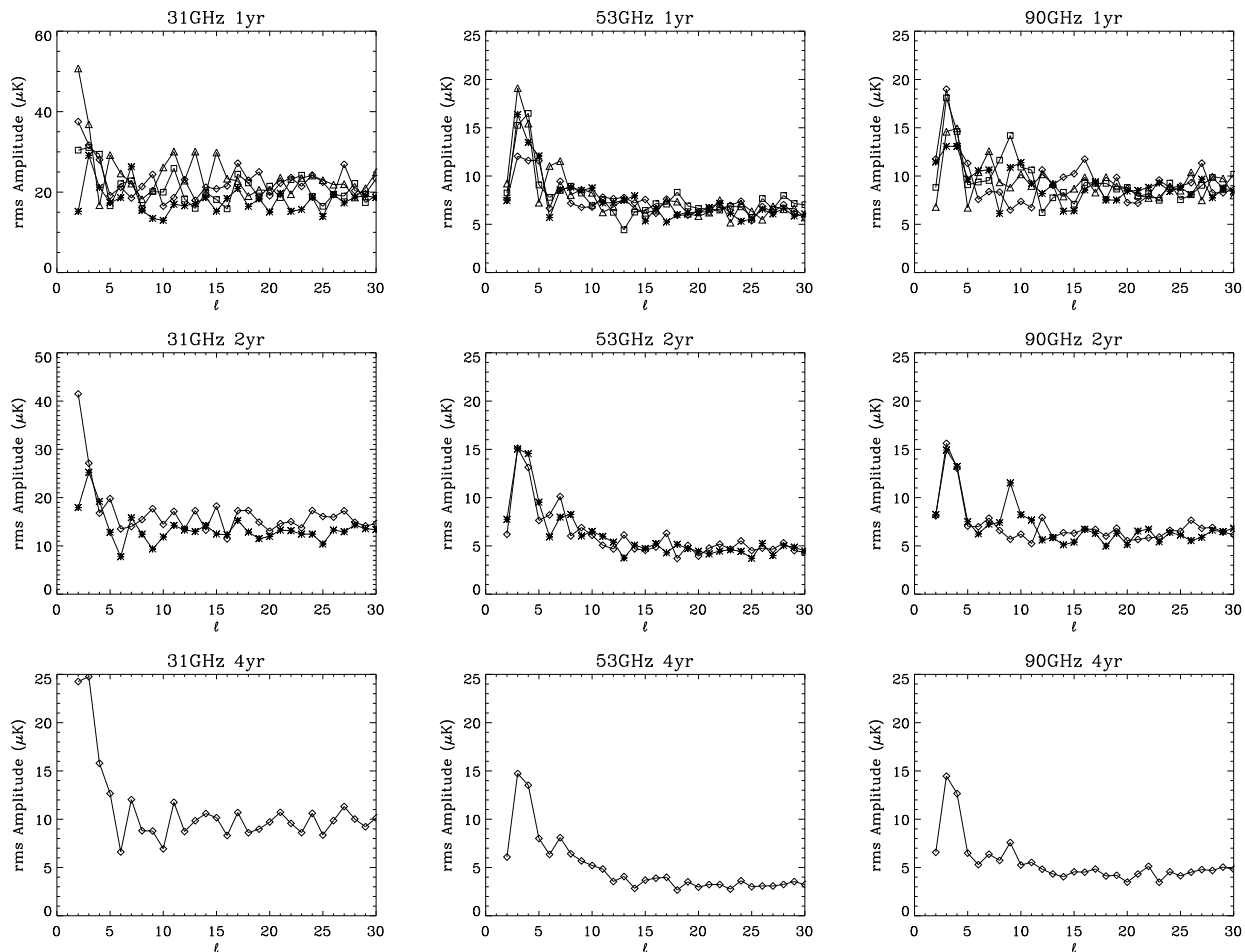


Figure 2: Power spectra of the DMR (galactic frame, extended Galaxy cut, 3881 pixels) inverse-noise-variance weighted sum maps, at each frequency of observations, for all yearly, 2-year, and 4-year sky maps (same coding as in Figure 1.) Variance weighting of the A and B sides makes the yearly and bi-yearly effective noise levels in the 31GHz map more consistent with one another than in the corresponding difference maps (with fifty-fifty noise contributions from the A and B sides), and the effective noise level in the sum maps somewhat lower than in the corresponding difference maps at all three frequencies.

of the sky maps. Both these goals are pursued within the mathematical framework for analysis of the DMR data which was originally described in [6], and [7]. I will briefly describe the DMR data, address the necessary technical points, and proceed to presentation of the results and discussion.

2 Data

The main result of the *COBE*-DMR mission is a set of full sky maps, comprised of two maps (A and B sides) at each frequency of 31.5, 53, and 90 GHz, pixelized in both galactic and ecliptic coordinates. The angular resolution of the instrument was $\sim 7^\circ$ FWHM, and the sky maps are divided into 6144 nearly equal area pixels.

A record of the sensitivity of each detector and the number of observations per pixel in each map are provided with the sky maps. This allows for stochastic modelling of the instrument noise, which is essential for a proper interpretation of the results of the data analysis and

subsequent inference of a parametric description for the cosmological signal. [Indeed, except for the dipole anisotropy and the galactic plane emission, the CMB anisotropy signals detected in the DMR maps are weak compared to typical noise contamination even at 53 GHz — rms signal $\sim 35 \mu\text{K}$ vs. rms noise $\sim 80 \mu\text{K}$ in a single pixel.]

Since the monitoring of the multichannel instrument performance was very long, DMR is to date unparalleled among the CMB anisotropy experiments in terms of noise control.

Using the customized Fourier tools introduced in [6] for the analysis of the incomplete sky of the Galaxy-excised DMR sky maps one can extract from the data the cut-sky power spectra of the sum and difference maps at each frequency, which are shown in Figures 1 and 2. Quantities plotted there are the rms values of the cut-sky harmonic coefficients (the usual $(2\ell + 1)$ degrees of freedom per ℓ -mode).

One should appreciate from Figure 1 the steady decrease with time ($\sim 1/\sqrt{t}$) of the rms noise amplitude, the excellent consistency of the yearly performances of the 53 and 90 GHz instruments, and very good consistency of the measured noise properties with the Gaussian model.

Figure 2 shows the power spectra of signal and noise. Even the totality of the 31.5 GHz data remains substantially noisier than the higher frequency channels, which together with uncertainties in the galactic foreground contribution renders its interpretation more problematic. Visual inspection of the 53 and 90 GHz power spectra provides a sense of strong consistency between these independent data sets.

3 Maximum likelihood estimation of the angular power spectrum of CMB anisotropy

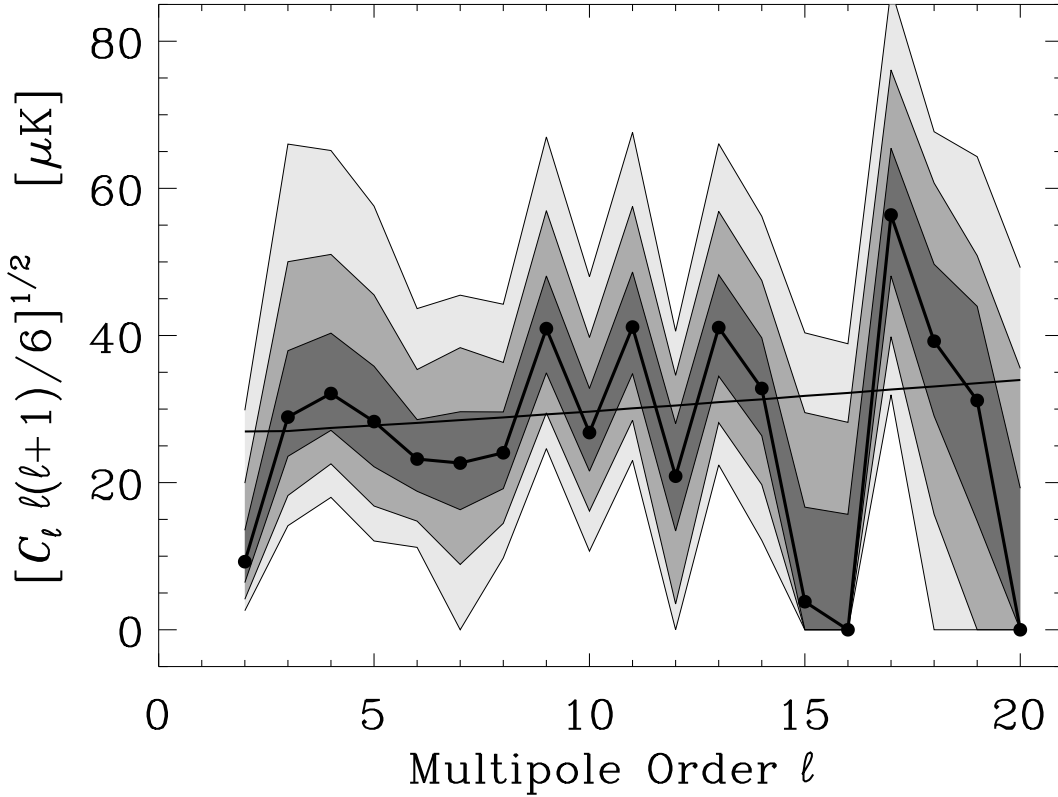
A method of cut-sky Fourier decomposition and maximum likelihood analysis of the DMR data to infer the parameters of a theoretical spectrum of CMB anisotropy was presented in [6]. The application of this formalism to derive the maximum likelihood estimates of the overall amplitude and shape parameters for power law spectrum fits to the 2-yr and 4-yr DMR data was given in [7], and [8], respectively. Here I demonstrate how this formalism allows one to derive a maximum likelihood estimate of the individual multipoles $C_\ell = \langle |a_{\ell m}|^2 \rangle = a_\ell^2$, where $\delta T/T(\Omega) = \sum_{\ell m} a_{\ell m} Y_{\ell m}(\Omega)$.

A proper analysis of a relatively complex data set such as DMR and the correct inference of a parametrisation of the sky distribution of CMB anisotropy requires the simultaneous treatment of several interrelated problems, which include:

- 1) incomplete sky coverage and resulting multipole coupling after excision of the galactic plane region from the analysed maps;
- 2) removal of the cosmologically irrelevant low order, $\ell = 0$, and 1 modes, preferably without affecting the higher order modes, which do carry cosmological information;
- 3) modeling of the nonuniform noise distribution;
- 4) identification and removal of possible diffuse foreground emission in the areas outside the galactic cut;
- 5) execution of an unbiased, or least-biased, parameter inference, preferably using the probability density which describes the tested model of anisotropy in an exact manner.

A program of analysis of the DMR data which addressed all of these points was conducted in [6], [7], and [8]. An important feature of this method of analysis is that it employs geometrically constructed orthogonalized spherical harmonics, which are *independent* of any cosmological theories that one might endeavour to test with the DMR data. This is radically different from the possible Karhunen-Loève type methods, where one builds the basis of modes for sky map

CMB Anisotropy Power Spectrum (Max.L. $\Delta\ell/\ell=0$)
COBE-DMR 4yr 53 and 90 GHz Data



K.M. Górski 1996

Figure 3: Power spectrum of the CMB anisotropy derived by the maximum likelihood method with each C_ℓ coefficient treated as a separate parameter (hence $\Delta\ell/\ell = 0$). Noise and incomplete sky coverage induce correlations, impossible to show on the plot, between the derived confidence intervals on each C_ℓ . One should note that a correct estimator of excess variance in signal over noise in the data was applied, hence no negative C_ℓ values were obtained. A low- ℓ tail of the CDM model CMB anisotropy spectrum (independently fitted to the same data) is shown as a slightly tilted solid line.

decomposition using a specific theoretical spectrum of CMB anisotropy (e.g. Bond and Jaffe in this volume).

Let us now establish how the method introduced in [6] can be used to compute an estimator of the full sky angular power spectrum, i.e. the coefficients C_ℓ which can be determined from the data. Since we work with the Fourier amplitudes \mathbf{c} which are linear combinations of pixel temperatures (as they are integrals on the cut-sky of the map products with the cut-sky orthogonalized spherical harmonic basis functions), their joint probability distribution is Gaussian (see [6] for formal details)

$$P(\mathbf{c}) d\mathbf{c} = \frac{d\mathbf{c}}{(2\pi)^{N/2} \sqrt{\det(\mathbf{S} + \mathbf{N})}} \exp\left(-\mathbf{c}^T \cdot (\mathbf{S} + \mathbf{N})^{-1} \cdot \mathbf{c} / 2\right), \quad (1)$$

where $\mathbf{C} = \mathbf{S} + \mathbf{N}$, and \mathbf{S} and \mathbf{N} are covariance matrices of the signal and noise, respectively. For the maximum likelihood calculations I use the likelihood function defined as

$$F(\mathbf{A}|\hat{\mathbf{c}}) = \det[\mathbf{S}(\mathbf{A}) + \mathbf{N}] + \hat{\mathbf{c}}^T \cdot [\mathbf{S}(\mathbf{A}) + \mathbf{N}]^{-1} \cdot \hat{\mathbf{c}}, \quad (2)$$

where the full sky signal variance matrix has the form

$$\mathbf{A} = \text{diag}[\underbrace{a_2^2, \dots, a_2^2}_{5 \text{ times}}, \underbrace{a_3^2, \dots, a_3^2}_{7 \text{ times}}, \dots, \underbrace{a_{\ell_{max}}^2, \dots, a_{\ell_{max}}^2}_{(2\ell_{max}+1) \text{ times}}]. \quad (3)$$

The maximum likelihood problem as formulated in eqs. (1-3) — seeking the coefficients C_2 - $C_{\ell_{max}}$ given the data vector $\hat{\mathbf{c}}$ — involves the assumption of a Gaussian distribution of both noise and CMB anisotropies, and the statistical isotropy of the field of temperature perturbations (hence only the ℓ dependence of $\langle |a_{\ell m}|^2 \rangle$), but does not imply any relation between C_ℓ -s at different values of ℓ — hence we are solving for the power spectrum of CMB anisotropy fully *independently* of any specific cosmological model.

A maximum likelihood search for the power spectrum that best matches the distribution of signal on the sky simply entails finding a minimum of the function $F(\mathbf{A})$ in the $\ell_{max} - 1$ -dimensional space. In the present case it is greatly facilitated by our ability to write down easily the expression for the gradient $\partial F / \partial a_\ell$, and implement a standard numerical routine for an extremum search with gradient zeroing. The solution to this problem for the DMR 4yr galactic frame data is shown in Figure 3. Our power spectrum estimator is really an estimator of excess variance in signal over noise in the data. One should note in Fig. 3 the asymmetry of the confidence intervals around the maximum likelihood solutions for the C_ℓ -s, and the fact that no derived values go negative. If there is no signal content in the data that can be attributed to a given C_ℓ , an upper limit is established, as e.g. for $\ell = 16$. The signal to noise ratio in Fourier space drops to ~ 1 at $\ell \sim 15$ in the DMR 4yr data. It is important to see that nearly all multipoles within that range are determined with great significance. As for the confidence intervals, the plot can not convey the notion of correlations between the errors on different multipoles. These correlations are quite small, and more significant for multipoles separated by $\Delta\ell = 2$ than otherwise. Because of the nontrivial (non-Gaussian) structure of confidence interval correlations it is difficult to implement an exact method of fitting of the theoretical model of CMB anisotropy to the DMR data by using the power spectrum, compressed rendition of the data. For such applications the accurate linear methods, as e.g. [7], should be preferred.

4 Linear filtering of the DMR sky maps

When the statistical properties of the signal, polluted by noise in the data, are known, one can apply powerful tools of image processing to improve, oftentimes visually quite dramatically, the presentation of the measurements. The best known device for linear filtering of noisy data is the celebrated Wiener filter. Alternatives, usually referred to as sub-optimal filters, do exist, and on occasion provide a preferred means of treating the noisy data. In the case of the DMR raw data the signal to noise ratio is pretty poor even in the 4yr data set. The Wiener filter, which practically “annihilates” those components of the data which are assessed to be noise dominated, when applied to data of low quality usually renders the impression of “over-smoothing”. I choose to apply another device, called the power-equalization filter, which is constructed as follows.

First let us define the measurement, signal, and noise vectors, and their covariance matrices:

$$\mathbf{m} = \mathbf{s} + \mathbf{n}, \quad \langle \mathbf{s} \cdot \mathbf{s}^T \rangle = \mathbf{S}, \quad \langle \mathbf{n} \cdot \mathbf{n}^T \rangle = \mathbf{N}, \quad \langle \mathbf{m} \cdot \mathbf{m}^T \rangle = \mathbf{S} + \mathbf{N}. \quad (4)$$

Next, define the filtered data vector, and the filter matrix:

$$\mathbf{f} = \mathbf{F} \cdot \mathbf{m} = \mathbf{F} \cdot (\mathbf{s} + \mathbf{n}). \quad (5)$$

If the filter is constructed from the requirement that the mean square deviation between the filtered and the true signal, $\epsilon = \langle (\mathbf{f} - \mathbf{s})^T \cdot (\mathbf{f} - \mathbf{s}) \rangle = \text{tr} \langle (\mathbf{f} - \mathbf{s}) \cdot (\mathbf{f} - \mathbf{s})^T \rangle$, is minimized, one obtains the Wiener filter

$$\mathbf{F}_W = \mathbf{S} \cdot (\mathbf{S} + \mathbf{N})^{-1}. \quad (6)$$

Another possibility for sub-optimal filtering, which renders the power equalization filter, arises when \mathbf{F} is chosen such that

$$\langle \mathbf{f} \cdot \mathbf{f}^T \rangle = \mathbf{S}, \quad \text{i.e.} \quad \mathbf{F}_{PE} \cdot (\mathbf{S} + \mathbf{N}) \cdot \mathbf{F}_{PE}^T = \mathbf{S}. \quad (7)$$

Equation (7) means that on average over many applications the power-equalization filter renders filtered data, whose statistical distribution matches that of the underlying signal.

Using Choleski decomposition of the relevant matrices, and the following auxiliary matrices, we can construct the power equalization filter as follows:

$$\mathbf{S}^{-1} = \mathbf{L}_{\mathbf{S}^{-1}} \cdot \mathbf{L}_{\mathbf{S}^{-1}}^T, \quad \mathbf{\Gamma}_{\mathbf{S}^{-1}} = \mathbf{L}_{\mathbf{S}^{-1}}^{-1}, \quad \mathbf{S} = \mathbf{\Gamma}_{\mathbf{S}^{-1}}^T \cdot \mathbf{\Gamma}_{\mathbf{S}^{-1}}, \quad (8)$$

$$(\mathbf{S} + \mathbf{N})^{-1} = \mathbf{L}_{(\mathbf{S} + \mathbf{N})^{-1}} \cdot \mathbf{L}_{(\mathbf{S} + \mathbf{N})^{-1}}^T, \quad \mathbf{\Gamma}_{(\mathbf{S} + \mathbf{N})^{-1}} = \mathbf{L}_{(\mathbf{S} + \mathbf{N})^{-1}}^{-1}, \quad \mathbf{S} + \mathbf{N} = \mathbf{\Gamma}_{(\mathbf{S} + \mathbf{N})^{-1}}^T \cdot \mathbf{\Gamma}_{(\mathbf{S} + \mathbf{N})^{-1}}, \quad (9)$$

and as a result:

$$\mathbf{F}_{PE} = \mathbf{\Gamma}_{\mathbf{S}^{-1}}^T \cdot \mathbf{L}_{(\mathbf{S} + \mathbf{N})^{-1}}^T \quad (10)$$

This is an upper triangular matrix, hence filtering of a given mode in the cut-sky data vector $\hat{\mathbf{c}}$ does not mix in the information from lower order modes, preserving the information ordering imposed by the construction of orthonormal modes (see [6]).

For the presentation purposes of this contribution I constructed separate filters for the DMR4 53 and 90 GHz maps. The tremendous advantage of DMR is clearly visible here. We can internally compare two sets of decent quality observations at 53 and 90 GHz, and we are able to quantify and visualize the consistency with which the instrument reveals the image of the last scattering surface.

5 The first image of last scattering surface

It should be realized that the *COBE*-DMR observations *did* allow us to make a first reliable picture of the last scattering surface. Recognition of this fact is somewhat obscured by the memory of the picture of the first DMR all sky map that was circulated in 1992 - a picture which was substantially distorted by noise features.

Four years after that presentation, the quality of DMR data is now substantially better, but it is still somewhat difficult to argue about its validity as an image of the last scattering surface, as there is simply no other data at microwave frequencies at the same angular scales to allow a direct image to image comparison with DMR. However, since DMR observed the sky at three frequencies, and two of these have rendered sky maps of decent quality, an internal image comparison is possible.

What I present here is a result of a fairly long chain of events: separate instruments (with different noise properties) were used to observe the sky (looking at different directions at the time of observations!), the data were separately analysed and corrected for the systematic effects, the maps were made separately, all the subsequent data reduction was performed separately, and in the end different filters were constructed and applied.

The end product of these operations is visible in two panels on the left side of the color plate as the DMR 53 and 90 GHz, power-equalisation filtered sky maps. To facilitate the comparison

and assessment of consistency of these maps I add and subtract them. This is shown in the remaining panels of the color plate in both Mollweide and spherical polar projections.

It is immediately clear that the 53 and 90 GHz maps contain many common features on large angular scales (and, as shown in [1], [11], [8], they can not be attributed to foreground emission from either the Galaxy, or nearby extragalactic objects). The epistemological value of this result of the *COBE*-DMR mission should not be underestimated, as this is the first time ever that we are afforded a reliable picture of the most remote regions of the universe. (I shall stress that I do not attempt to make an argument about the wonders of image processing, but about our truly good luck with the DMR's splendid performance at two different frequencies!)

The rms anisotropy in the $(53 + 90)/2$ PE filtered map is $35\mu\text{K}$, while the rms in the $(53 - 90)/2$ map is about $15\mu\text{K}$. These numbers define the accuracy to which *COBE*-DMR has revealed to us a most elusive astronomical realm, and provided a first direct glimpse at the universe in its embryonic state.

Acknowledgements. I gratefully acknowledge the efforts of the *COBE* team and the support of the Office of Space Sciences at NASA. I am grateful to A.J. Banday for help with preparation of the manuscript.

References

- [1] Banday A.J. *et al.*, 1996, *Astrophys. J.* **468**, L85
- [2] Banday A.J. *et al.*, 1997, *Astrophys. J.* in press
- [3] Bennett C.L. *et al.*, 1994, *Astrophys. J.* **436**, 423
- [4] Bennett C.L. *et al.*, 1996, *Astrophys. J.* **464**, L1
- [5] Bunn, E., & White, M., 1996, *astro-ph* 960735
- [6] Górski K.M., 1994, *Astrophys. J.* **430**, L85
- [7] Górski K.M. *et al.*, 1994, *Astrophys. J.* **430**, L89
- [8] Górski K.M. *et al.*, 1996, *Astrophys. J.* **464**, L11
- [9] Hinshaw G. *et al.*, 1996, *Astrophys. J.* **464**, L25
- [10] Hinshaw G. *et al.*, 1996, *Astrophys. J.* **464**, L17
- [11] Kogut A. *et al.*, 1996, *Astrophys. J.* **464**, L5
- [12] Kogut A. *et al.*, 1996, *Astrophys. J.* **464**, L29
- [13] Kogut A. *et al.*, 1996, *Astrophys. J.* **470**, 653
- [14] Smoot G.F. *et al.*, 1992, *Astrophys. J.* **396**, L1
- [15] Tegmark M., 1996, *Astrophys. J.* **464**, L34
- [16] Wright, E.L., 1996, *Astrophys. J.* **464**, L21

This figure "color_plot.gif" is available in "gif" format from:

<http://arxiv.org/ps/astro-ph/9701191v1>